

Deciphering the spectra of breast cancer in multispectral optoacoustic tomography

Maximilian Bader^{a,b}, Benedict E. Mc Larney^c, Katja Pinker^{d,e}, Jan Grimm^{c,d,f,g,h}, Dominik Jüstel^{a,b,i},
Vasilis Ntziachristos^{a,b,j,✉}

^aChair of Biological Imaging at the Central Institute for Translational Cancer Research (TranslaTUM), School of Medicine and Health, Technical University of Munich, Munich, Germany

^bInstitute of Biological and Medical Imaging, Helmholtz Zentrum München, Neuherberg, Germany

^cMolecular Pharmacology Program, Memorial Sloan Kettering Cancer Center, New York, USA

^dDepartment of Radiology, Memorial Sloan Kettering Cancer Center, New York, USA

^eDepartment of Radiology, Columbia University Vagelos College of Physicians and Surgeons, New York, USA

^fDepartment of Pharmacology, Weill Cornell Medicine, New York, USA

^gDepartment of Radiology, Weill Cornell Medicine, New York, USA

^hMolecular Imaging Therapy Service, Memorial Sloan Kettering Cancer Center, New York, USA

ⁱInstitute of Computational Biology, Helmholtz Zentrum München, Neuherberg, Germany

^jMunich Institute of Robotics and Machine Intelligence (MIRMI), Technical University of Munich, Munich, Germany

✉bioimaging.translatum@tum.de, Address: Technical University of Munich, Chair of Biological Imaging, Ismaninger Straße 22, D-81675 Munich, Germany

ABSTRACT

Multispectral optoacoustic tomography (MSOT) has been utilized to non-invasively resolve morphological changes like angiogenesis and metabolic parameters like hemoglobin concentration and oxygenation in breast tumors. Compared to other optical methods, MSOT provides higher spatial resolution, higher penetration depth and does not require the use of contrast agents. Thus, MSOT could aid the non-invasive diagnosis and treatment monitoring of breast cancer. Because MSOT illuminates tissue at multiple wavelengths, the acquired data contains spectral information about the chromophores contained in tissue. This spectral data may serve as additional dimension to infer cancer biomarkers. Recent advances in data processing and image reconstruction enable the spectroscopic analysis of MSOT data. However, effects like fluence attenuation and spectral coloring alter the spectral data hampering the identification of chromophores. Hence, it is necessary to analyze and understand spectral MSOT data—"MSOT spectra"—to not draw wrong conclusions.

In this work, we showcase MSOT spectra of healthy and cancerous breast tissue in four patients between 680 nm and 1100 nm for the first time. We investigate trends and variations in MSOT spectra of tumor, tumor core, tumor rim, tumor perimeter and healthy background tissue with respect to different regions of interest and with respect to the tumors' molecular subtypes. Moreover, we showcase effects of spectral coloring which are observed in the in-vivo MSOT spectra.

Our work provides a new perspective on MSOT imaging of breast cancer. We lay the foundation to derive novel, spectral MSOT biomarkers of breast cancer aiding the clinical translation.

Keywords: Multispectral optoacoustic tomography, in vivo imaging, breast cancer, photoacoustic imaging, spectroscopy

1. INTRODUCTION

Breast cancer is one of the major applications researched in optoacoustic (OptA) imaging. Out of the 20 in-human OptA imaging studies with the highest number of participants, eight have focused on breast cancer.¹ Multispectral Optoacoustic Tomography (MSOT), which performs OptA imaging with optical illumination at varying wavelengths in the near-infrared (NIR), has been shown to non-invasively resolve morphological changes like angiogenesis²⁻⁴ and metabolic parameters like oxygenation⁵⁻¹¹ in breast tumors. Combined MSOT with ultrasound (US) imaging, so-called hybrid Multispectral Optoacoustic Tomography and Ultrasound imaging (MS-OPUS), provides tissue morphological and metabolic parameters, which may aid cancer diagnosis and treatment planning and monitoring.¹²⁻¹⁶ We have recently shown that advanced image formation and data preprocessing methods enable high contrast and high fidelity OptA imaging of breast cancer,^{16,17} lymph nodes,¹⁸ thyroid cancer,¹⁹ and peripheral nerves.²⁰ Going beyond imaging with high morphological and structural fidelity, the advanced methods allow us to assess the high-resolution spectral MSOT data—"MSOT spectra," which may allow us to infer novel breast cancer biomarkers.²¹

However, the analysis and interpretation of MSOT spectra are challenging. MSOT spectra are the product of local absorption and local optical fluence. Therefore, MSOT spectra vary strongly compared to the optical absorption spectra of tissue chromophores. Moreover, with the optical fluence dependent on the surrounding tissue, the inversion to obtain chromophore concentrations from MSOT spectra is highly ill-posed.^{22,23} As a consequence, MSOT spectra are difficult to interpret, and it remains challenging to reliably infer cancer biomarkers like local tissue oxygenation from MSOT spectra.

Many clinical, in-human breast studies have employed OptA imaging with dual-wavelength illumination to assess variations in tissue oxygenation as a cancer biomarker.^{6-11,24} However, sampling tissue spectra at two wavelengths allows us to determine at most two tissue chromophores. Additionally, it remains doubtful if chromophores can even be accurately quantified in humans due to spectral coloring in tissue.²³ MSOT, with illumination between 700 nm and 980nm, has been shown to display the distribution of water and lipids in addition to angiogenesis and oxygenation-related parameters in cancerous and healthy breast tissue.^{5,16} While MSOT spectra of vascularization in the tumor perimeter, ducts, and inflammation foci in single patients were displayed,¹⁶ no specific comparison of MSOT spectra of the cancerous and healthy breast tissue was performed.

We hypothesize that recent data processing and image formation advances leading to high-quality OptA images with spectral stability enable the analysis and interpretation of MSOT spectra of cancerous and healthy breast tissue.

In this work, we showcase MSOT spectra of healthy and cancerous breast tissue in four patients between 680 nm and 1100 nm for the first time. We investigate trends and variations in MSOT spectra of tumor, tumor core, tumor rim, tumor perimeter, and healthy background tissue with respect to different regions of interest and tumor types. Moreover, we investigate the effects of spectral coloring in in-vivo MSOT spectra. By comparing MSOT spectra of healthy and cancerous breast tissue and describing the impact of spectral coloring, we provide an intuition for MSOT spectra and aid their interpretation and the derivation of breast cancer biomarkers.

2. METHODS

Data Acquisition and Study Protocol

In the clinical study, twelve breast cancer patients were imaged with a hybrid MS-OPUS device, a custom MSOT Acuity Echo® prototype (iThera Medical GmbH, Munich, Germany), at Memorial Sloan Kettering Cancer Center, New York City, New York, USA. Following the principle displayed in Fig. 1, multiple cross-sectional OptA and US tumor images were acquired by a senior radiologist specializing in breast cancer ultrasonography for all patients. The handheld probe was pressed against the breast. Then, laser illumination caused the emission of acoustic waves in highly absorbing tissue like blood vessels in the tumor environment due to the optoacoustic effect. The radiologist also imaged the ipsilateral, contralateral healthy breast and the axilla for comparison with the cancerous tissue. The patients underwent biopsies, and the diagnosis served as the ground truth label for tumor malignancy and type. The study was approved by the ethics committee of the Memorial Sloan Kettering Cancer Center institutional review board (IRB number Rad21-003). The

hybrid MS-OPUS device utilized a pulsed, wavelength-tunable laser (660-1300 nm) with a 25 Hz repetition rate and a pulse duration of 5 ns. The maximum energy output of 13 mJ at 700 nm complied with the safety regulations for skin exposure by the American National Standards Institute.²⁵ The device comprised an arc-shaped concave US transducer array of 256 elements with 125° angular coverage and 4 cm arc radius. The elements were cylindrically focused into the imaging plane. The acquisition system had a center frequency of approximately 3.6 MHz, 111% bandwidth, and a sampling rate of 40 MHz. Images were acquired between 660 nm and 1130 nm with a step size of 10 nm (48 wavelengths). US images were co-registered with the OptA images at a frame rate of approximately 6.25 Hz using the Synthetic Transmit Aperture protocol. A single scan containing multiple multispectral frames, i.e., sets of images at all acquired wavelengths, was acquired at each scanning position.

Data Processing and Image Reconstruction

As Fig. 1 shows, the MS-OPUS device provides raw MSOT signal data and US images automatically reconstructed using a Delay-and-Sum algorithm with a 200 μm resolution. Subsequently, we determined two multispectral frames with lowest motion in each scan employing Motion score, a fully automatic algorithm that estimates motion in the frames based on the US images. The multispectral OptA frames determined by Motion score exhibit low morphological distortions and spectral corruptions caused by motion during the scan which is beneficial for further data analysis.²⁶ Before OptA image reconstruction, the acquired signal data of the selected two selected multispectral frames was corrected for laser energy fluctuations, and a deep-learning-based denoising of the MSOT signal data was applied.¹⁷ The denoised MSOT signal data was band-pass filtered (300 kHz / 700 kHz – 12 MHz), and images were formed using a custom model-based reconstruction algorithm using an individual synthetic total impulse response (isTIR) approach with a dual speed of sound at a resolution of 100 μm.^{27,28} The model combines a measured individual electrical impulse response for each transducer in the US detector and a simulated spatial pulse response (SPR) comprising the spatial impulse response of the transducers and the wave shape of a spherically symmetric OptA absorber with Gaussian profile (standard deviation: 50μm).^{29,30} The algorithm solves a non-negativity-constrained least squares problem with a Shearlet-L¹ regularizer.^{18,19,31,32} The regularization parameters were determined via the L-curve. US image quality was enhanced by first compounding, i.e., averaging all US images corresponding to an individual multispectral frame. Afterward, the reconstructed US image was finally co-registered with the OptA image at 800nm with an affine transformation.¹⁶

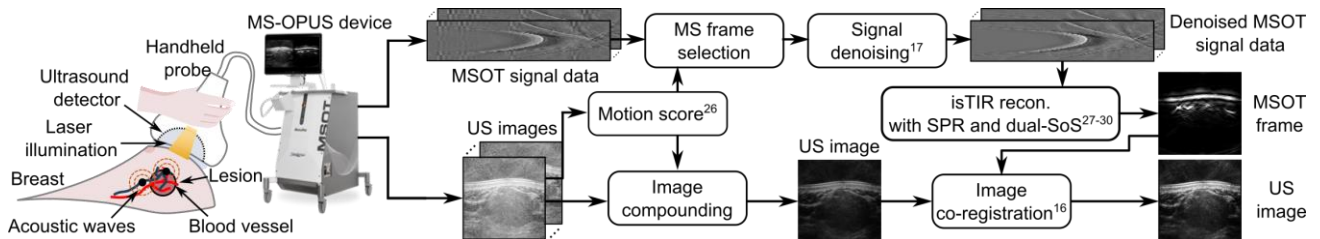


Figure 1 Hybrid Multispectral Optoacoustic Tomography and Ultrasound imaging (MS-OPUS) of breast cancer and the advanced signal processing and image formation techniques. Schematic of the procedure to acquire a multispectral optoacoustic (MSOT) frame, i.e., optoacoustic images at multiple wavelengths and a co-registered ultrasound (US) image of a tumor lesion in the breast with a hybrid MS-OPUS device (MSOT Acuity Echo CE®, iThera Medical GmbH, Munich, Germany). The system provides MSOT signal data and reconstructed US images. Based on the US images, Motion score²⁶ selects the multispectral (MS) frames with the least motion. The MSOT signal data is then denoised¹⁷ to remove electrical noise and reconstructed with a reconstruction (recon) algorithm to obtain the MSOT frame. The algorithm uses an individual total synthetic impulse response (isTIR) model with a dual speed of sound (SoS) and spatial pulse response (SPR).²⁷⁻³⁰ US images of an MS frame are compounded and then co-registered to the MSOT frame.¹⁶

Image Visualization and Data Analysis

For all patients, tumors were segmented in the US image by a specialist in OptA imaging under the guidance of a radiologist using ImageJ. For further spectral analysis, a specialist in OptA imaging selected scans of four patients with high image quality, one patient with a malignant tumor and three patients with benign tumors. The image quality was assessed in terms of motion in the frame, depth of the tumor, appearance of artifacts, and overall contrast in the image. For image visualization, we created an individual US image, a dual-band OptA image at 800 nm blending images bandpass filtered with 300 kHz – 12 MHz and the 700 kHz – 12 MHz, as well as a blend of single-band OptA images acquired at 700 nm and 880 nm (bandpass filter: 700 kHz – 12MHz). We applied local contrast normalization and

sigmoid normalization on the images before blending.¹⁶ For spectral analysis, the tumor-related ROIs, namely tumor, tumor core, tumor rim, tumor perimeter, and a healthy background, were segmented in the MSOT and US images by a specialist using ImageJ. The healthy background was segmented on the side of the image inside healthy tissue at the same depth as the tumor. Moreover, a subcutaneous artery and an artery deep next to the tumor were selected in a single case. Only the spectra of images with 700 kHz – 12 MHz bandpass filter and wavelengths ranging from 680 nm to 1100 nm were further analyzed. The MSOT spectra of the different ROIs were pooled with a two-dimensional Gaussian kernel (standard deviation: 50 μ m) using Python and Numpy. We then computed a set of quantiles symmetric around the median (0.01, 0.05, 0.1, 0.15, 0.2, 0.25, 0.3, 0.4, 0.45, 0.5, 0.55, 0.6, 0.65, 0.7, 0.75, 0.8, 0.85, 0.9, 0.95, 0.99), the median and the mean of all pixel spectra in an ROI to analyze and visualize the MSOT spectra. We selected the mean ROI spectrum for each patient to compare the ROI spectra over multiple patients.

3. RESULTS

High-resolution MS-OPUS images and MSOT spectra of healthy and cancerous breast tissue

Fig. 2 shows the high-quality MS-OPUS images of a representative case, a solid papillary carcinoma (malignant). The MSOT spectra pooled from the large US-based healthy and cancerous ROIs are broadly distributed such that a mean or median spectrum cannot accurately represent the distribution. However, for smaller, well-defined ROIs, like blood vessels, the spectra distribution is narrow, such that the mean and median spectra are representative. Even effects of fluence decay over depth and spectral coloring can be observed.

The cross-sectional US image in Fig. 2a prominently displays the tumor morphology (yellow dashed line). Fig 2b, the dual-band OptA image at 800 nm (isosbestic point of oxygenated and deoxygenated hemoglobin), showcases vascularization up to a depth of approximately 1.8cm. Superficially, and on the tumor perimeter, prominent small vessels are visible in yellow. Inside the tumor and deep in the center of the image, bulky contrast appears in red. The single-band OptA image blend at 700 nm (blue) and 880 nm (pink) in Fig. 2c shows the long, thin vessels in the tumor environment in purple, indicating that these vessels are arteries because oxygenated hemoglobin (HbO₂) absorbs light stronger at 880nm than deoxygenated hemoglobin (Hb). On the other hand, tissue appearing in blue either has a strong melanin concentration like the skin or seems to be rich in Hb, with the absorption of Hb and melanin exceeding the absorption of other tissue chromophores. While the long, thin vessels in the tumor perimeter appear in strong purple, blue contrast appears inside the tumor. The OptA images display no prominent ring artifacts caused by electrical signal noise despite the lack of frame or wavelength averaging.

Fig. 2d-h feature the spectra distribution (inter-percentile range: gray shaded area), as well as the median (blue line) and mean (orange dashed line) for the tumor (d), the tumor core (e), the tumor rim (f), the tumor perimeter (g), and the healthy background (h). For the tumor in Fig. 2d, the tumor core in Fig. 2e, and the tumor rim in Fig. 2f, the spectra distribution and the mean and median spectra do not show any differences qualitatively. For all three ROIs, the spectra distribution is very wide, with the 1st and 99th percentile residing below 0.1 and above 20, respectively. The mean and median spectra stay approximately constant between 680 nm and 800 nm and steadily decay for wavelength from 800 nm to 1100 nm. The spectra distribution is even wider for the tumor perimeter in Fig. 2g, especially between 45th and 55th percentile. The mean and median spectra appear qualitatively similar to the mean MSOT spectra of the tumor, tumor core, and tumor rim. However, the decline for wavelengths larger than 800 nm appears less prominent. The mean and median spectra of the healthy background in Fig. 2h show a local maximum around 980 nm.

Fig 2i,j show the MSOT spectrum of arteries 1 and 2 (see Fig. 2b) respectively. For both arteries, the spectra distribution is very narrow and smooth, showing no sudden spikes or notches. Because the spectra distributions are narrow, the mean and median spectra represent the spectra distribution. Qualitatively, the mean spectrum of artery 1 is very similar to the optical absorption spectrum of HbO₂. The spectra distribution of artery 2, located deeper in tissue than artery 1, has a lower amplitude than for artery 1. Moreover, the spectrum of artery 2 starts declining for wavelengths larger than 850 nm and shows a distinctive notch at 930 nm. This decline in amplitude and deformation for large wavelengths can be attributed to the decay of fluence in tissue and the related spectral coloring.

The advanced data processing methods provide high-quality MSOT images, which allow us to capitalize on the MSOT spectra for biomarker inference. In small ROIs like blood vessels, the MSOT spectra are very stable, so variations over depth can be assessed, and interpretation is possible. However, in large US-based ROIs like the tumor, the spectra are

very heterogeneous, and an averaged mean spectrum does not accurately represent the spectra distribution. Interpreting the averaged mean MSOT spectra is challenging, and the averaging may cover subtle spectra variations caused by diseases.

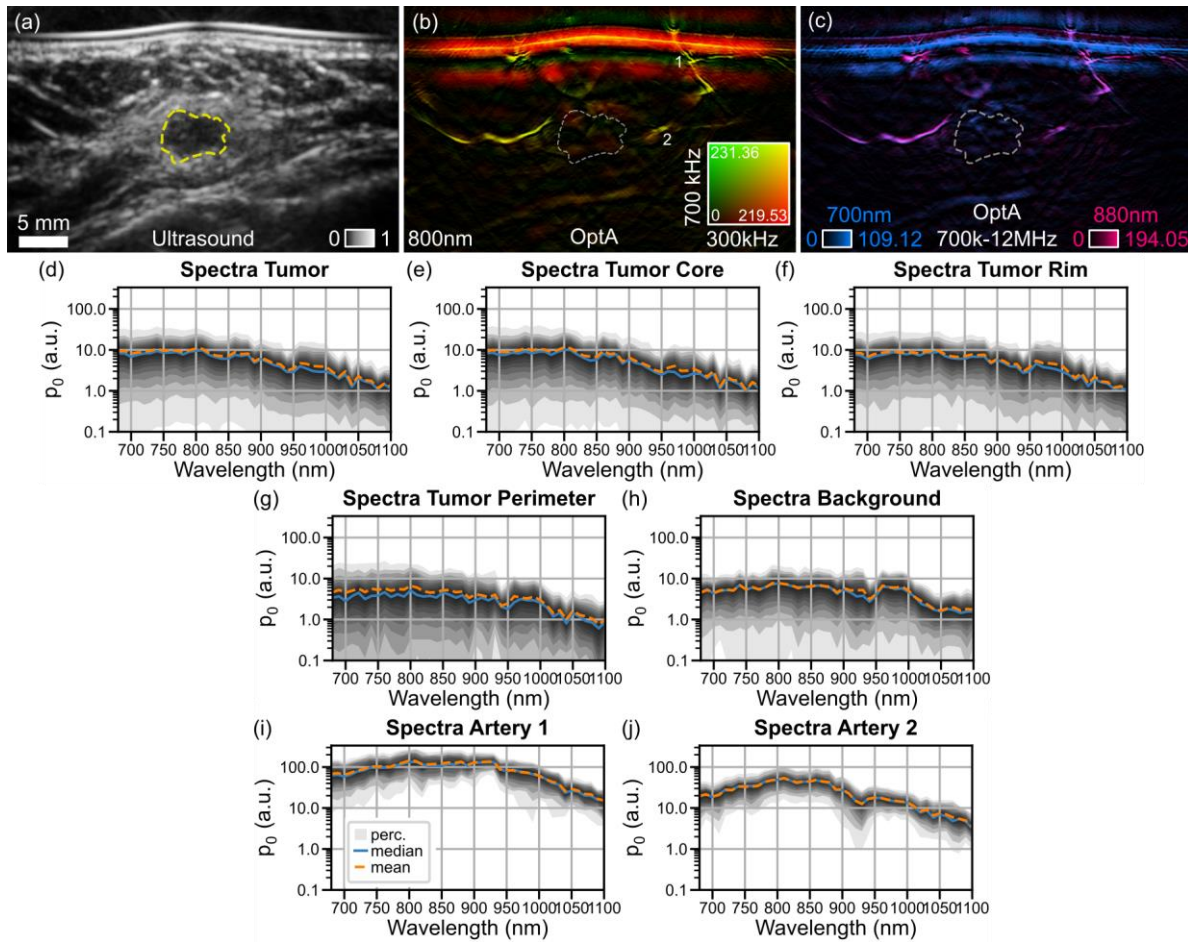


Figure 2 Breast cancer images and spectra acquired with hybrid Multispectral Optoacoustic Tomography and ultrasound imaging (MS-OPUS). (a) The ultrasound image of a solid papillary carcinoma, a malignant mamma carcinoma (dashed yellow line). (b) The co-registered dual-band optoacoustic (OptA) image at 800nm showcases enhanced vasculature in the tumor environment and superficially (1,2: arteries at different depths). Dual-band OptA images display bulk structures in red and fine structures in yellow. (c) The single-band OptA image blend at 700nm (blue) and 880nm (red) shows vascular structures and skin lines. Arteries are expected to appear in red or purple, and veins, as well as hypoxic tissue, in blue. The skin appears blue as well. All images (a-c) display the same field of view with the scale bar corresponding to 5 mm length. (d) The distribution of MSOT spectra (gray shading), median (blue dashed line), and mean MSOT spectra (orange dashed line) of the tumor (see Fig. 2a-c). The distribution is visualized by shading different inter-percentile ranges. The darkness increases when the range between the percentiles decreases. The mean and median spectra do not represent the spectra distribution as the distribution is widespread. (e-h) The spectra distribution for ROIs tumor core (e), tumor rim (f), tumor perimeter (g), and healthy background (h) are widespread like for the whole tumor (d), and mean as well as median spectra are not representative. (i) The spectra distribution for artery 1 (see Fig. 2b) shows a higher amplitude than the tumor-related ROI spectra distributions. The distribution is very narrow, and mean and median spectra are representative. The spectrum qualitatively matches the optical absorption spectrum of oxygenated hemoglobin. (j) The MSOT spectra distribution of artery 2 shows a lower amplitude and a local minimum at 930 nm compared to the spectra distribution of artery 1. Abbreviations: p_0 —initial pressure, a.u.—arbitrary unit.

Mean MSOT spectra of cancerous and healthy breast tissue in four patients

Fig. 3 displays the mean MSOT spectra averaged over ROIs in healthy and cancerous breast tissue for four cases. Based on the mean MSOT spectra of ROIs in healthy and cancerous breast tissue, neither differences between healthy and cancerous breast tissue or benign and malignant tumors can be observed.

The mean MSOT spectrum averaged across the tumor in four different cases is displayed in Fig. 3a. The mean MSOT spectra of case 1 (black), 2 (blue), and 3 (orange) have very similar shapes and mean MSOT spectra in case 1 and 2 show a local maximum 980 nm. The spectrum of case 4 (green) differs strongly from the mean MSOT spectra of the three other cases. Furthermore, no differences between the single malignant tumor (case 1) and the three benign tumors (cases 2-4) can be observed because the variation between case 4 and cases 1-3 is substantially larger. Fig. 3b,c display the mean MSOT spectra averaged over tumor core (b) and tumor rim (c) in the four cases, respectively. For example, tumor cases 1-3 have similar spectra, while the spectrum of case 4 varies significantly. No differences between the tumor spectra, core, and rim can be observed. The mean MSOT spectra averaged across the tumor perimeter in the four cases can be observed in Fig. 3d. The mean MSOT spectra show more substantial agreement between the four cases than the mean MSOT spectra in the tumor, tumor core, and tumor rim. Fig. 3e shows the four cases' mean MSOT spectra averaged over the healthy background. In case 4, the mean spectrum differs strongly from the mean MSOT spectra of the other three patients, like in the tumor, the tumor core, and the tumor rim before. The mean MSOT spectra averaged over the healthy background tissue do not show any qualitative differences compared to the tumor-related ROIs.

The mean MSOT spectra do not show differences between healthy and cancerous tissue or benign and malignant tumors. However, in a single case (see Fig. 2), we observed that the mean MSOT spectrum does not represent the spectra distribution in large ROIs like the tumor or the background. Consequently, a simple statistical analysis comparing large ROIs' mean MSOT spectra is insufficient to obtain breast cancer biomarkers from MSOT images.

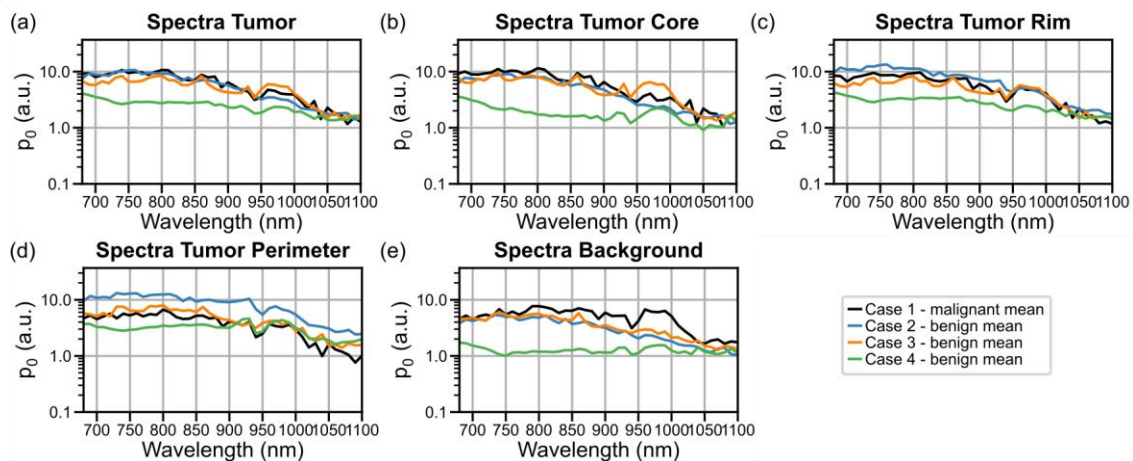


Figure 3 Analysis of Mean Multispectral Optoacoustic Tomography (MSOT) spectra of four patients. (a-e) The mean MSOT spectra averaged over the tumor ROI (a) of case 1 (black, malignant tumor, see Fig. 2 for individual spectra distributions), case 2 (blue, benign tumor) and case 3 (orange, benign tumor) are all steady up to 800 nm and decline for larger wavelengths. The mean spectrum for case 4 (green, benign tumor) is much lower in amplitude than the spectrum of all other cases. Cases 1, 3 and 4 show a small local maximum at 980 nm, but no differences between benign and malignant tumors is visible. The mean MSOT spectra averaged over the tumor core (b), the tumor rim (c), and the tumor perimeter (d) all have very similar shapes. Only the mean MSOT spectra of case 4 show lower amplitude than the spectra of all other cases. The mean spectrum of healthy background of case 1, 2 and 3 is very similar, but only shows a distinctive local maximum at 980 nm for case 1. Case 4 has a qualitatively completely different mean spectrum like for all other ROIs. No qualitative differences can be observed between mean MSOT spectra of healthy and cancerous ROIs, which are consistent across cases. Abbreviations: p_0 —initial pressure, a.u.—arbitrary unit.

4. DISCUSSION

We demonstrated that our advanced data processing and image formation methods provide high-quality MSOT images and enable the reliable analysis of MSOT spectra. In well-defined small ROIs like blood vessels, MSOT spectra are stable and easy to interpret such that even effects of fluence attenuation and spectral coloring can be clearly observed. However, for large ROIs like tumors, the spectra vary strongly. The mean MSOT spectra averaged over large ROIs in cancerous and healthy breast tissue show qualitatively no differences for multiple patients with different tumors. In previous work, MSOT spectra were compared to observe relative changes in chromophores, like blood oxygenation,⁶⁻¹⁰ raw MSOT spectra of breast tissue have not yet been investigated. By showcasing and analyzing MSOT spectra distributions and averages across multiple ROIs, we provide clinicians and researchers with an intuition for MSOT spectra, aiding the interpretation of any biomarkers derived from MSOT spectra.

In a single representative case, we showcased the MSOT distributions in different healthy and cancerous ROIs in breast tissue ranging from 680 nm to 1100 nm. Previous MSOT imaging in breast cancer had been limited to wavelengths up to 980 nm,^{5,16} but extending the optical illumination into the second NIR window (up to 1100nm) may improve the spectral stability and allow deeper tissue penetration due to the low optical scattering in breast tissue at these wavelengths.³³ We observed narrow MSOT spectra distributions for small ROIs like blood vessels, demonstrating the consistency of MSOT spectra in homogeneous tissue at the same depth. In the presence of electrical ring noise or motion in a multispectral frame, the MSOT spectra feature non-biological spikes and notches, diminishing the spectral consistency.^{17,26} The consistency of MSOT spectra also facilitated the reliable analysis of spectral coloring, because the changes in MSOT spectra of blood vessels with depth appeared deterministically. The overall reduction in initial pressure amplitude with depth matched the expectation of decreasing optical fluence with depth.^{34,35} The distinctive notch in the spectra of the deep artery at 930 nm could be interpreted as spectral deformation due to spectral coloring by lipids. Lipid is one of the major chromophores in breast tissue and exhibits a distinctive absorption peak at 930 nm.³⁶ Given the light traveled multiple millimeters through healthy breast tissue before reaching the vessel, the optical fluence at the vessel's depth was lower at 930 nm than at other wavelengths, resulting in a lower MSOT spectra amplitude. Spectral coloring is one of the major factors impeding quantitative OptA imaging today.³⁴ General fluence correction methods^{34,37} and specific methods to accurately estimate blood oxygenation in MSOT images³⁸⁻⁴⁰ have been introduced. Still, these methods often only perform accurately in simulations, phantoms, or animal imaging but cannot be transferred to human MSOT imaging with a handheld probe.

Other than for small ROIs, the MSOT spectra distribution of large ROIs like tumor, the tumor core, the tumor rim, the tumor perimeter, and the healthy background, the MSOT spectra distribution was very wide and showed less consistency than in smaller ROIs. The large variability in large ROIs may be caused by large ROI capturing multiple tissues with different absorption spectra.⁴¹ However, fluence decay and spectral coloring expected with depth cause MSOT spectra variations in such large ROIs.³⁴ Most importantly, though, the mean or median MSOT spectra do not represent the whole distribution.

Comparing the mean spectra of cancerous and healthy breast tissue in four patients, no consistent differences in the spectra were observed. The same applied to comparing the mean spectra of benign and malignant tumors. However, as observed in a single case, the mean spectrum averaged over a large ROI was not representative of the MSOT spectra distribution in this ROI. Consequently, subtle or local variations might have been overlooked in solely comparing the mean spectra averaged over large tumor ROIs. Therefore, it has been proposed to look for qualitative image features besides mean spectra¹⁹ and, perform data-driven unmixing and investigate spectral correlations beyond the mean.²⁰

By showcasing raw MSOT spectra of breast cancer and methodically analyzing the MSOT spectra shape and their stability over ROIs, we aid scientists and physicians in interpreting raw MSOT spectra and derived biomarkers. We established that raw MSOT spectra in breast cancer could be utilized to infer breast cancer biomarkers from MSOT spectra, but comprehensive statistics beyond the mean are required to identify subtle and local spectral variations due to diseases. However, our analysis was limited to only four patients, which does not cover the large variety of molecular changes that breast cancer induces in tissue. Moreover, we could not recover explicit chromophore concentrations in tissue because we performed no fluence correction methods. Instead, we're limiting the work to the qualitative analysis of MSOT spectra. Finally, we analyzed the spectra of images with fine vascular networks without large bulk structures because we reconstructed the images with a high-pass filter cutoff at 700 kHz. Therefore, we omit any changes in bulk tissue, such as lipid pads induced by cancer, and primarily focus on finer structures like vascularization.

Our work aids the understanding and interpretation of MSOT spectra of breast cancer. Because we analyze raw MSOT spectra instead of computing spectra-based biomarkers, we provide a new perspective on MSOT imaging of breast cancer. We lay the foundation for spectral MSOT analysis and the resulting derivation of breast cancer biomarkers from MSOT images, aiding the clinical translation.

ACKNOWLEDGEMENTS

The research leading to these results has received funding from the Deutsche Forschungsgemeinschaft (DFG) - 455422993 as part of the Research Unit FOR 5298 (iMAGO, subproject TP2, GZ: NT 3/32-1) and from the Sonderforschungsbereich-824 (SFB-824), subproject A1 and the European Research Council (ERC) under the European Union's Horizon 2020 research and innovation programme under grant agreement No 694968 (PREMSOT). M.B. has also received financial travel support from the Internationalization program of the Technical University of Munich Graduate School and the SPIE Student Conference Support Program.

The authors would like to thank Lukas Imanuel Scheel-Platz for his fruitful input on the visual and written presentation of the results.

REFERENCES

- [1] Ntziachristos, V., "Addressing unmet clinical need with optoacoustic imaging," *Nature Reviews Bioengineering* (2024).
- [2] Ermilov, S. A., Khamapirad, T., Conjusteau, A., Leonard, M. H., Lacewell, R., Mehta, K., Miller, T. and Oraevsky, A. A., "Laser optoacoustic imaging system for detection of breast cancer," *J Biomed Opt* 14(2), 024007 (2009).
- [3] Heijblom, M., Piras, D., Engh, F. M. Van Den, Van der Schaaf, M., Klaase, J. M., Steenberg, W. and Manohar, S., "The state of the art in breast imaging using the Twente Photoacoustic Mammoscope : results from 31 measurements on malignancies," *Eur Radiol* 26, 3874–3887 (2016).
- [4] Lin, L., Hu, P., Shi, J., Appleton, C. M., Maslov, K., Li, L., Zhang, R. and Wang, L. V., "Single-breath-hold photoacoustic computed tomography of the breast," *Nat Commun* 9 (2018).
- [5] Diot, G., Metz, S., Noske, A., Liapis, E., Schroeder, B., Ovsepian, S. V., Meier, R., Rummeny, E. and Ntziachristos, V., "Multispectral Optoacoustic Tomography (MSOT) of human breast cancer," *Clinical Cancer Research* 23(22), 6912–6922 (2017).
- [6] Neuschler, E. I., Butler, R. S., Young, C. A., Barke, L. D., Bertrand, M. L., Böhm-Vélez, M., Destounis, S., Donlan, P., Grobmyer, S. R., Katzen, J., Kist, K. A., Lavin, P. T., Makariou, E. V., Parris, T. M., Schilling, K. J., Tucker, F. L. and Dogan, B. E., "A pivotal study of optoacoustic imaging to diagnose benign and malignant breast masses: A new evaluation tool for radiologists," *Radiology* 287(2), 398–412 (2018).
- [7] Neuschler, E. I., Lavin, P. T., Tucker, F. L., Barke, L. D., Bertrand, M. L., Böhm-vélez, M., Destounis, S., Dogan, B. E., Grobmyer, S. R., Katzen, J., Kist, K. A., Makariou, E. V., Parris, T. M., Young, C. A. and Butler, R. S., "Downgrading and Upgrading Gray-Scale Ultrasound BI-RADS Categories of Benign and Malignant Masses With Optoacoustics: A Pilot Study," *American Journal of Roentgenology* 211(3), 689–700 (2018).
- [8] Butler, R. S., Lavin, P. T., Tucker, F. L., Barke, L. D., Böhm-vélez, M., Katzen, J., Kist, K. A., Makariou, E. V., Schilling, K. J., Young, C. A., Dogan, B. E. and Neuschler, E. I., "Optoacoustic Breast Imaging: Imaging-Pathology Correlation of Optoacoustic Features in Benign and Malignant Breast Masses," *American Journal of Roentgenology* 211(5), 1155–1170 (2018).
- [9] Dogan, B. E., Menezes, G. L. G., Butler, R. S., Neuschler, E. I., Aitchison, R., Lavin, P. T., Tucker, F. L., Grobmyer, S. R., Otto, P. M. and Stavros, A. T., "Optoacoustic imaging and gray-scale us features of breast cancers: Correlation with molecular subtypes," *Radiology* 292(3), 564–572 (2019).

- [10] Seiler, S. J., Neuschler, E. I., Butler, R. S., Lavin, P. T. and Dogan, B. E., "Optoacoustic Imaging With Decision Support for Differentiation of Benign and Malignant Breast Masses: A 15-Reader Retrospective Study," *American Journal of Roentgenology* 220(5), 646–658 (2023).
- [11] Huang, Z., Mo, S., Wu, H., Kong, Y., Luo, H., Li, G., Zheng, J., Tian, H., Tang, S., Chen, Z., Wang, Y., Xu, J., Zhou, L. and Dong, F., "Optimizing Breast Cancer Diagnosis with Photoacoustic Imaging: An Analysis of Intratumoral and Peritumoral Radiomics," *Photoacoustics* 38(April), 100606 (2024).
- [12] Weissleder, R., "Molecular imaging in cancer," *Science* (1979) 312(5777), 1168–1171 (2006).
- [13] Tromberg, B. J., Cerussi, A., Shah, N., Compton, M., Durkin, A., Hsiang, D., Butler, J. and Mehta, R., "Imaging in breast cancer: Diffuse optics in breast cancer: detecting tumors in pre-menopausal women and monitoring neoadjuvant chemotherapy," *Breast Cancer Research* 7(6), 279 (2005).
- [14] Brindle, K., "New approaches for imaging tumour responses to treatment," *Nat Rev Cancer* 8(2), 94–107 (2008).
- [15] Lin, L., Tong, X., Hu, P., Invernizzi, M., Lai, L. and Wang, L. V., "Photoacoustic Computed Tomography of Breast Cancer in Response to Neoadjuvant Chemotherapy," *Advanced Science* 8(7), 1–10 (2021).
- [16] Kukačka, J., Metz, S., Dehner, C., Muckenhuber, A., Paul-Yuan, K., Karlas, A., Fallenberg, E. M., Rummeny, E., Jüstel, D. and Ntziachristos, V., "Image processing improvements afford second-generation handheld optoacoustic imaging of breast cancer patients," *Photoacoustics* 26(February) (2022).
- [17] Dehner, C., Olefir, I., Chowdhury, K. B., Justel, D. and Ntziachristos, V., "Deep-learning-based electrical noise removal enables high spectral optoacoustic contrast in deep tissue," *IEEE Trans Med Imaging* 41(11), 3182–3193 (2022).
- [18] Vonk, J., Kukačka, J., Steinkamp, P. J., de Wit, J. G., Voskuil, F. J., Hooghiemstra, W. T. R., Bader, M., Jüstel, D., Ntziachristos, V., van Dam, G. M. and Witjes, M. J. H., "Multispectral optoacoustic tomography for in vivo detection of lymph node metastases in oral cancer patients using an EGFR-targeted contrast agent and intrinsic tissue contrast: A proof-of-concept study," *Photoacoustics* 26 (2022).
- [19] Noltes, M. E., Bader, M., Metman, M. J. H., Vonk, J., Steinkamp, P. J., Kukačka, J., Westerlaan, H. E., Dierckx, R. A. J. O., van Hemel, B. M., Brouwers, A. H., van Dam, G. M., Jüstel, D., Ntziachristos, V. and Kruijff, S., "Towards in vivo characterization of thyroid nodules suspicious for malignancy using multispectral optoacoustic tomography," *Eur J Nucl Med Mol Imaging* (2023).
- [20] Jüstel, D., Irl, H., Hinterwimmer, F., Dehner, C., Simson, W., Navab, N., Schneider, G. and Ntziachristos, V., "Spotlight on nerves: Portable multispectral optoacoustic imaging of peripheral nerve vascularization and morphology," *Advanced Science* 2301322, 1–14 (2023).
- [21] Manohar, S. and Dantuma, M., "Current and future trends in photoacoustic breast imaging," *Photoacoustics* 16(September 2018), 100134 (2019).
- [22] Cox, B. T., Laufer, J. G., Arridge, S. R. and Beard, P. C., "Quantitative spectroscopic photoacoustic imaging: a review," *J Biomed Opt* 17(6), 061202 (2012).
- [23] Hochuli, R., An, L., Beard, P. C. and Cox, B. T., "Estimating blood oxygenation from photoacoustic images: can a simple linear spectroscopic inversion ever work?," *J Biomed Opt* 24(12), 1 (2019).
- [24] Li, J., Chen, Y., Ye, W., Zhang, M., Zhu, J., Zhi, W. and Cheng, Q., "Molecular breast cancer subtype identification using photoacoustic spectral analysis and machine learning at the biomacromolecular level," *Photoacoustics* 30, 100483 (2023).
- [25] ANSI Inc., [American national standard for the safe use of lasers], Laser Institute of America, Orlando (2007).
- [26] Kukačka, J., "Advancing Clinical Optoacoustic Tomography," PhD (2024).
- [27] Chowdhury, K. B., Prakash, J., Karlas, A., Justel, D. and Ntziachristos, V., "A Synthetic Total Impulse Response Characterization Method for Correction of Hand-Held Optoacoustic Images," *IEEE Trans Med Imaging* 39(10), 3218–3230 (2020).

- [28] Chowdhury, K. B., Bader, M., Dehner, C., Jüstel, D. and Ntziachristos, V., "Individual transducer impulse response characterization method to improve image quality of array-based handheld optoacoustic tomography," *Opt Lett* 46(1), 1 (2021).
- [29] Englert, L., Jüstel, D. and Ntziachristos, V., "The need for optoacoustic microscopy," *Review of Modern Physics* 96 (2024).
- [30] Bader, M., Haim, P., Scheel-Platz, L. I., Karlas, A., Irl, H., Ntziachristos, V. and Jüstel, D., "Spatial Pulse Response - A Precise Numerical Simulation of Optoacoustic Wave Detection with Arbitrarily Shaped Transducers," *ArXiv* (2023).
- [31] Kutyniok, G. and Lim, W. Q., "Compactly supported shearlets are optimally sparse," *J Approx Theory* 163(11), 1564–1589 (2011).
- [32] Wright, S. J., Nowak, R. D. and Figueiredo, M. A. T., "Sparse reconstruction by separable approximation," *IEEE Transactions on Signal Processing* 57(7), 2479–2493 (2009).
- [33] Upputuri, P. K. and Pramanik, M., "Photoacoustic imaging in the second near-infrared window: a review," *J Biomed Opt* 24(04), 1 (2019).
- [34] Cox, B. T., Laufer, J. G., Arridge, S. R. and Beard, P. C., "Quantitative spectroscopic photoacoustic imaging: a review," *J Biomed Opt* 17(6), 061202 (2012).
- [35] Park, J., Choi, S., Knieling, F., Clingman, B., Bohndiek, S. E., Wang, L. V. and Kim, C., "Clinical translation of photoacoustic imaging," *Nature Reviews Bioengineering* (2024).
- [36] Vogt, W. C., Jia, C., Wear, K. A., Garra, B. S. and Joshua Pfefer, T., "Biologically relevant photoacoustic imaging phantoms with tunable optical and acoustic properties," *J Biomed Opt* 21(10), 101405 (2016).
- [37] Zhou, X., Akhlaghi, N., Wear, K. A., Garra, B. S., Pfefer, T. J. and Vogt, W. C., "Evaluation of Fluence Correction Algorithms in Multispectral Photoacoustic Imaging," *Photoacoustics* 19(April), 100181 (2020).
- [38] Tzoumas, S., Nunes, A., Olefir, I., Stangl, S., Symvoulidis, P., Glasl, S., Bayer, C., Multhoff, G. and Ntziachristos, V., "Eigenspectra optoacoustic tomography achieves quantitative blood oxygenation imaging deep in tissues," *Nat Commun* 7(May), 1–10 (2016).
- [39] Gröhl, J., Kirchner, T., Adler, T. J., Hacker, L., Holzwarth, N., Hernández-Aguilera, A., Herrera, M. A., Santos, E., Bohndiek, S. E. and Maier-Hein, L., "Learned spectral decoloring enables photoacoustic oximetry," *Sci Rep* 11(1), 1–12 (2021).
- [40] Nolke, J. H., Adler, T. J., Schellenberg, M., Dreher, K. K., Holzwarth, N., Bender, C. J., Tizabi, M. D., Seitel, A. and Maier-Hein, L., "Photoacoustic quantification of tissue oxygenation using conditional invertible neural networks," *IEEE Trans Med Imaging* XX(Xx) (2024).
- [41] Park, S., Villa, U., Li, F., Cam, R. M., Oraevsky, A. A. and Anastasio, M. A., "Stochastic three-dimensional numerical phantoms to enable computational studies in quantitative optoacoustic computed tomography of breast cancer," *J Biomed Opt* 28(06) (2023).